1 **Revision 2**

2 **Raman and IR studies of the effect of Fe substitution in hydroxyapatites and**

3 **deuterated hydroxyapatite**

4      Anastasios Antonakos[1], Efthymios Liarokapis[1], Andreas Kyriacou[2], and Theodora

5                                      Leventouri[2]

6      [1]Department of Physics, National Technical University of Athens, 15780 Athens,

7      Greece

8      [2]Physics Department, Florida Atlantic University, Boca Raton, FL 33431, USA

9                                      **Abstract**

10    We have studied synthetic Fe-substituted hydroxyapatite $Ca_{5-x}Fe_x(PO_4)_3OH$ and the

11    corresponding deuterated samples with varying Fe concentrations $x$ ($0 \leq x \leq 0.3$) by Raman

12    and IR spectroscopy at room temperature. In the IR spectra, substitution of deuterons for

13    protons affects the OH internal mode in a way consistent with the mass difference of the

14    substituting ions, as well as a mode attributed to vibrations of the $Ca_3$-(OH) unit. In the

15    Raman spectra, the frequency of all modes is not noticeably affected by the Fe

16    substitution. Raman bands show increased width and substantial reduction in intensity

17    with increasing amount of Fe, presumably related to disorder introduced by the

18    substitution. We find that the disorder is smaller in the hydroxyapatites compared to the

19    deuterated ones.

20

21    Keywords: hydroxyapatites, Fe-substitution, Raman spectroscopy, FTIR

## Introduction

22

23     Iron is a biologically important trace element substituting for Ca in the hydroxyapatite

24     (HAp) structure (0.003 wt% in enamel, 0.01 – 0.1 wt% in bone). It has been

25     demonstrated that Fe-deficient rat bones exhibit decreased mechanical strength,

26     decreased bone mass density, and increased fragility (Medeiros et al. 2002), whereas Fe

27     overload leads to decreased osteoblast cell number and activity (De Vernejoul et al.

28     1984). Disagreements on the structural modifications and related properties that the Fe

29     for Ca substitution causes in the apatite lattice are reported in the literature (Wu et al.

30     2007; Low et al. 2008; Khudolozhkin et al. 1974; Morissay et al. 2005; Jiang et al. 2002;

31     Li et al. 2012; Salviulo et al. 2011). In a recent publication we have shown that Fe

32     substitutes at both Ca(1) and Ca(2) crystallographic sites with a preference at the Ca(2)

33     site by applying simultaneous Rietveld refinement of X-ray diffraction (XRD) and

34     neutron powder diffraction (NPD) powder patterns of Fe-substituted, deuterated (FeDAp)

35     powder samples (Kyriakou et al. 2013).

36     Here we present Raman and FTIR studies of the same series of FeHAp and FeDAp

37     powder samples. We have studied the effect of the deuteron substitution for H on certain

38     modes and compared experimental results with first principles calculations (Corno et al.

39     2006; Pedone et al. 2007; Calderin et al. 2005; Ulian et al. 2013). Our results indicate that

40     Fe substitution strongly affects the intensity of the internal modes of the $PO_4$ tetrahedra,

41     due to the lattice distortion introduced by Fe at the Ca sites. Furthermore, it is found that

42     the disorder in the lattice of deuterated hydroxyapatites is more sensitive to the Fe

43     substitution.

44 **Experimental**

45 The powder compounds studied have the chemical form $Ca_{5-x}Fe_x(PO_4)_3OH$ (FeHAp)

46 with Fe atomic concentration $0 \leq x \leq 0.3$). A similar set had been deuterated in flowing

47 oxygen-enriched $D_2O$ at $600^o$ C (FeDAp). Table 1 lists the composition of the

48 investigated samples. A 0.2 M solution of $Ca(NO_3)_2.4H_2O$ (99.98% ALPHA AESAR)

49 was added drop wise to a 0.12 M solution of $(NH_4)_2PO_4.4H_2O$ (99.99% ALDRICH) at

50 ambient conditions. The pH was maintained at $9.5 \pm 0.1$ by adding $NH_4OH$.

51 Hydroxyapatite was formed according to the reaction:

$$5Ca(NO_3)_2 + 3(NH_4)_2HPO_4 \xrightarrow{NH_4OH} Ca_5(PO_4)_3OH$$
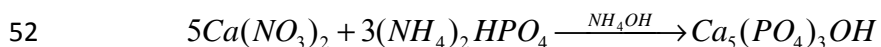
53 Then, $FeCl_2.4H_2O$ solution, heated to 85 $^oC$, was added drop wise to the HAp solution.

54 Fe-substituted HAp formed according to the reaction:

$$Ca_5(PO_4)_3OH + xFeCl_2 \longrightarrow Ca_{5-x}Fe_x(PO_4)_3OH$$

56 The final precipitate was aged for 20 h, washed, dried and heat-treated in a tube furnace

57 at 650 ºC for 15 h under flowing $N_2$ to prevent oxidation of the Fe ions.

58 Detailed information on the preparation conditions and characterization from

59 simultaneous Rietveld refinements of X-ray and neutron powder diffraction, x-ray

60 diffraction (XRD), transmitted electron microscopy (TEM), and magnetometry methods

61 has been published elsewhere (Kyriakou et al. 2013). A mixture of irregularly shaped

62 rods and spherical particles with dimensions between 15 nm and 65 nm was observed in

63 the TEM image of FeHAp0, while the size range is limited to 20 to 50 nm in the FeDAp0

64  sample. When Fe substitutes for Ca, the size range and shapes of the samples remain

65  unaltered regardless of the Fe concentration $x$.

66      Micro-Raman spectra were obtained at room temperature using a T64000 Jobin-Yvon

67  triple spectrometer, equipped with a liquid nitrogen cooled Charge Coupled Device

68  (CCD) and a microscope. The 514.5 nm wavelength of an $Ar^+$ laser was used for

69  excitation in a backscattering geometry of the sample under the microscope. The

70  spectrum accumulation time was 3 hours and the laser power at the sample was 0.2 mW.

71  The spectrometer was calibrated before and after each measurement using a silicon wafer

72  or a reference Kr lamp. Because of the random orientation of the microcrystals in the

73  powder samples, no exact selection rules could be applied. The selection rules could give

74  only limited information about the properties of the Raman tensors because of the random

75  orientation of the microcrystallites in the powder samples. The differentiation of

76  orientation was studied by turning the sample stage between $0^o$ to $90^o$ while no

77  dependence was found by changing the polarization of the laser. Therefore, the spectra of

78  all samples were recorded with random polarization. The ×100 (N.A. 0.95) and ×50

79  (N.A. 0.80) magnification lenses were employed for the Raman measurements with the

80  laser spot focussed to ~1μm and ~2μm, respectively. Theoretically one would expect a

81  20% larger spot for the ×50 magnification and roughly two times larger confocal volume.

82  The confocal configuration of the spectrometer, together with the micrometric probe size,

83  reduces the fluorescence problems encountered in the conventional Raman spectroscopy

84  of such materials (Penel et al. 1998; Okazaki and Takahashi 1997; Wopenka and Pasteris

85  2005).

4

86    The Fourier transform infrared (FTIR) spectra were recorded using a Bruker Optic

87    IFS66v/S interferometer equipped with a MIRacle™ Single Reflection ATR (Attenuated

88    Total Reflectance) unit with a diamond/ZnSe crystal plate. The range of frequencies was

89    525 to 4000 $cm^{-1}$, and the spectra were recorded at ambient conditions with a resolution

90    of 2 $cm^{-1}$. In order to obtain a good signal-to-noise ratio, 1200 scans were collected and

91    averaged. A KBr beam splitter was used for the M-IR source. The ATR unit permits

92    spectra collection without any specific sample preparation, but only for the region above

93    525 $cm^{-1}$. A high-pressure lamp has been used in order to achieve high spectral quality

94    and to avoid low pressure effects. Since the pressure effect of the ATR accessory could

95    not be measured, an empirical method was used whereby the variations of intensities and

96    the ratio of the intensities were considered as a function of pressure; they increase to a

97    maximum and then remain fairly constant as the applied force is increased further.

98    **Results and discussion**

99    Figure 1a presents the ATR FTIR spectra of all samples in the high frequency region.

100    The continuous line spectra correspond to the as prepared FeHAp samples, and the dotted

101    ones to the deuterated FeDAp samples. The sharp band at ~3572 $cm^{-1}$ in the FeHAp

102    spectra for all Fe concentrations is assigned to the OH stretching mode (Elliott 1994). The

103    mode frequency is mostly related to the mass of the H and therefore, D substitution for H

104    should modify its frequency mainly according to the mass ratio of the two H isotopes.

105    The absence of this mode from the FeDAps and the appearance of a sharp band at ~2633

106    $cm^{-1}$ confirms the deuteration of the samples. In particular, the frequency of this band

107    follows approximately the mass rule

108
$$\omega_{D\text{-}O} = \omega_{H\text{-}O}\,(M_{D\text{-}O}/M_{H\text{-}O})^{1/2}$$

109       Figure 1b shows the lower frequency part of the ATR FTIR spectra of all samples.

110    Several peaks appear, located at ~566, 600, 631, 963, 1026, and ~1088 cm$^{-1}$. Of these

111    modes, only that at ~631 is affected by the deuteron substitution, while the remainder are

112    not noticeably modified. Some small changes in frequency of the ~1026 cm$^{-1}$ peak are

113    most likely due to intensity modifications of those modes that contribute to this peak. The

114    first two modes at ~566 and ~600 cm$^{-1}$ have been attributed to the $v_4$ doubly degenerate

115    asymmetric O-P-O bending mode of the $PO_4$ tetrahedron (Antonakos et al. 2007). The

116    higher frequency peaks at 1026, and ~1088 cm$^{-1}$ are related to the $v_3$ triply degenerate

117    asymmetric P-O stretching mode of the $PO_4$ tetrahedron (Antonakos et al. 2007). The

118    weak but sharp band at 963 cm$^{-1}$ can be assigned to the $v_1$ vibration (symmetric P-O

119    stretching mode) of the $PO_4$ tetrahedron (Penel et al. 1998; Antonakos et al. 2007, Park et

120    al. 2002). Finally, the weak mode at ~631 cm$^{-1}$ has been attributed to the OH librational

121    mode of the Ca3-OH group, i.e. the OH ion straddles across the Ca triangles that are

122    situated on the mirror plane of the apatite structure (Cant et al. 1971, Elliott 1994;

123    Antonakos et al. 2007). Some *ab initio* calculations assign this mode to the internal $v_4$

124    vibrations (Corno et al. 2006; Pedone et al. 2007). This does not appear to be correct,

125    since this mode disappears almost completely on deuteration, and is neither affected in

126    intensity nor width by the Fe substitution. As we will see below in the Raman spectra, Fe

127    substitution reduces substantially the intensity and increases the width of the internal

128    vibration modes of the $PO_4$ tetrahedron. Therefore, the mode must be related to the OH

129    librational vibration of the $Ca_3$-(OH) group. Unfortunately, ATR did not allow lower

130    frequency measurements to follow the mode in the expected frequency from the mass

131    difference H-D. Table 2 presents the detected IR and Raman modes and their assignment

132    (Elliott 1994; Antonakos et al. 2007).

133        Figure 2 presents data with ×100 (dotted line) and ×50 (continuous line)

134    magnifications for the low (Fig. 2a) and high (Fig. 2b) frequency regions. Although in

135    our previous investigations of apatite higher magnification gave stronger peaks

136    (Antonakos et al. 2007), this did not occur in this study, presumably due to the diffused

137    light by the nanostructured samples that favors the longer focusing. Several peaks can be

138    discriminated mainly with the ×50 magnification. In the low frequency part (Fig. 2a)

139    these are located at ~330 $cm^{-1}$ (very weak) and ~431, 448, 581, 593, 610, and ~617 $cm^{-1}$

140    (strong ones). The two strong ones at ~431 and ~448 $cm^{-1}$ have been assigned to $\nu_2$

141    vibrations, while the other four modes at higher frequency belong to the $\nu_4$ mode of the

142    $PO_4$ group. The origin of the weak mode at ~330 $cm^{-1}$ will be discussed below. In the

143    high frequency region (Fig. 2b) the peaks are located at ~839, 894, 916, 925, 962, 1027,

144    1040, 1046, 1075, 1122, 1252, and 1297 $cm^{-1}$. Most of them can be only observed with

145    the ×50 magnification. From those peaks, the ones at ~1027, 1040, 1046, and ~1075 $cm^{-1}$

146    have been assigned by several authors to the $\nu_3$ vibrations, and the one at ~962 $cm^{-1}$ to $\nu_1$

147    of the $PO_4$ unit (Antonakos et al. 2007). The lower frequency modes (843 – 925 $cm^{-1}$) are

148    related neither to Fe introduced to the sample nor to an Fe oxide impurity since they are

149    not modified in intensity by increasing the amount of Fe. Modes at relative frequencies

150    have been proposed in shell model lattice dynamic calculations (Calderin et al. 2005), but

151    other more recent theoretical calculations did not find any modes related to the undoped

152    HAp in this frequency region (Corno et al. 2006; Pedone et al. 2007; Ulian et al. 2013).

153    Most likely the bands at 843 and 894 $cm^{-1}$ are related to atmospheric $CO_3^{-2}$ ions entering

7

154    the HAp structure during the sample preparation. Similar results were obtained in other

155    studies (Leventouri at al. 2003; Antonakos et al. 2007). Then the two broad bands at

156    ~1252 and ~1297 cm$^{-1}$ are related to $CO_3^{-2}$/amide and/or $HPO_4^{-2}$ impurities (Vignoles-

157    Montrejaud 1984; Penel et al. 1998; Antonakos et al. 2007). Finally, the very narrow

158    band at ~1122 cm$^{-1}$ is a signal from the fluorescence lamp.

159       Figure 3 shows the effect of the 0.30 atomic nominal Fe substitution for Ca

160    corresponding to the two magnifications. In the low frequency region (Fig. 3a) all strong

161    modes that appear in the pure HAp spectrum completely disappear, while new peaks

162    appear located at ~224, 244, 291, 409, and ~498 cm$^{-1}$. All of them belong to hematite (de

163    Faria et al. 1997). A peak at ~612 cm$^{-1}$ is mainly from the strong hematite band, which

164    masks the narrow weaker $\nu_4$ $PO_4$ peaks of the HAp (seen in Fig.2a). The lower frequency

165    part of Figure 3b (843 – 925 cm$^{-1}$) and the $\nu_1$ $PO_4$ mode remain practically unchanged in

166    intensity. The $\nu_3$ $PO_4$ modes are damped and broaden due to disorder introduced by the Fe

167    substitution. The $\nu_3$ $PO_4$ region was found in previous studies to be very sensitive upon

168    substitution due to the different HAp environments present (Elliott 1994, Penel et al.

169    1998, Antonakos et al. 2007). At higher frequency, a new strong broad band develops

170    upon Fe substitution at 1320 cm$^{-1}$. This band is expected to appear strong when excited

171    with the 514 nm laser and is related to $\alpha$-$Fe_2O_3$ (hematite) (Wang et al. 2005). Although

172    this band was observed previously, the explanation for the wavelength response behavior

173    and for its origin is still unclear, and may be caused by a two magnon scattering process

174    (Martin et al. 1977) or a resonance-enhanced two-phonon scattering process (McCarty et

175    al. 1988; Massey et al. 1990; Shim and Duffy 2001). The fundamental mode could be the

176    660 cm$^{-1}$ IR active Eu band of hematite and therefore an overtone.

177    The evolution of the Raman spectra with increasing Fe substitution is presented in

178    Figure 4a for the low frequency part of FeDAps. It is observed that the intensity of the

179    modes assigned to hematite (marked by straight lines) increase with the amount of Fe

180    substitution, as presented in Figure 4b. On the one hand, XRD results have detected

181    traces of increasing amounts of hematite starting from the x = 0.20 nominal atomic

182    substitution (Kyriakou et al. 2013). On the other hand, Raman spectroscopy that is more

183    sensitive to detect impurities indicates that the hematite phase is present in all Fe

184    substituted compounds, even for x = 0.05 (Fig.4b). The intensity of the modes assigned to

185    internal vibrations of the $PO_4$ tetrahedra (marked by arrows) continuously decreases with

186    increasing amounts of Fe, and almost completely disappears for the 0.02 atomic nominal

187    Fe substitution for Ca. The comparison of Figure 2a (x = 0) with Figure 3a (x = 0.3)

188    shows that the effect is similar for the as-prepared set of samples (FeHAp). In the low

189    frequency region of the Raman spectra, a mode of E1 symmetry related to Ca-OH is

190    expected at 330 $cm^{-1}$ (Pedone et al. 2007). A mode at close frequency (332 $cm^{-1}$) is

191    observed in pure DAp, which gradually disappears with Fe substitution (Fig.4a). This

192    mode involves vibrations of OH. Therefore, the D substitution would affect (decrease) its

193    frequency. In Figure 2a (HAp), this mode appears unshifted at the same frequency, hence,

194    questioning its assignment to vibrations that involve the OH units (Pedone et al. 2007).

195    The Fe substitution for Ca could introduce disorder by the breaking of long-range

196    symmetry and shifting to lower frequencies of the modes involving the Ca atoms owing

197    to their mass difference. The internal modes of the $PO_4$ units should not be affected

198    significantly. Except from a substantial reduction in intensity (Fig.4a), the internal modes

199    are not modified in frequency, probably because of the only small amounts of Fe (up to

200    0.3 atomic, nominal content).

201        Depending on the mass difference between the substituting (Fe) and the original

202    (Ca) atom, the compound could follow one or two mode behaviors (Srivastava 1990). In

203    the former case, there will be a gradual shift in frequency towards the limiting value of a

204    hypothetical system with 100% Fe at the Ca site. In the latter, there will be a gradual

205    development of another mode that will correspond to the frequency of the hypothetical

206    end member. Due to the different coordination of the substituting Fe, it is very unlikely to

207    assume one-mode behavior, since the internal modes of $PO_4$ will be affected only

208    indirectly by the breaking of the external bonds to the Ca sites. Concerning the effect of

209    the mass difference between Fe and Ca on the vibrational modes, *ab initio* calculations

210    have investigated $^{42}Ca$ isotopic substitution for $^{40}Ca$ (5% mass difference at the Ca sites)

211    and deuteration (Corno et al. 2006). It has been found (Corno et al. 2006), that the

212    expected frequency shifts for modes above ~600 cm$^{-1}$ will not exceed ~1 cm$^{-1}$. Only

213    Raman bands of frequency less than ~400 cm$^{-1}$ are expected to be shifted by a few cm$^{-1}$

214    (Corno et al. 2006). In our case, even for x = 0.30 (6% atomic Fe substitution for Ca)

215    there will only be a 2.5% mass difference with the partial substitution of Fe for Ca.

216    Therefore, the mass effect on the vibration frequencies will be even smaller. Concerning

217    deuteration, only peaks in the range ~600 cm$^{-1}$ are expected to be shifter substantially

218    (Corno et al. 2006). From the observed modes in both IR and Raman spectra, only the

219    above-mentioned mode at ~631 cm$^{-1}$ is affected, but, as previously discussed, should be

220    correlated to an OH vibrational mode and not a $PO_4$ one (Fig.1b). The rest of the modes

221    appear at the same frequency in both HAp and DAp (Figs.1b, 2, & 4a).

222    What is impressive is the strong reduction in intensity of the majority of the

223    modes in the Raman spectra (Figs. 4a and 5) even with such small amounts of Fe

224    substitution (maximum nominal atomic amount 6%). As found by Kyriakou et al. (2013),

225    $Fe^{3+}$ appears in a fourfold coordination breaking some bonds with the O(2) and O(3)

226    nearest neighbors, while $Fe^{+2}$ is in a sixfold coordination breaking the bond with O(1).

227    The difference in mass between the two elements (Fe and Ca) cannot justify such

228    disorder, as similar differences in mass without any chemical variation usually modify the

229    phonon characteristics, without inducing disorder. We can recognize disorder from the

230    increase in the modes width and the reduction in its intensity. The variation of disorder

231    with doping is depicted in Figure 6 for the stronger $v_1$ $PO_4$ mode at ~962 cm$^{-1}$ and both

232    isotopic compounds. It can be observed that in FeHAp there is a continuous decrease in

233    intensity and, at the same time, substantial increase in width with a characteristic change

234    in behavior at $x \sim 0.2$ (Fig.6a). On the other hand, FeDAp appears to become disordered

235    faster, reaching the same asymptotic tendency at $x \sim 0.1$ (Fig. 6b). This behavior

236    characterizes the other internal modes of the $PO_4$ tetrahedron, as shown in Figure 7.

237    Again, in the FeHAp samples there is a slower continuous decrease in intensity than in

238    FeDAp. Refinements of the XRD patterns for FeHAp and FeDAp revealed the same Fe

239    content for same nominal x and therefore the differences in the disorder could not be due

240    to differing amounts of Fe concentration in the two sample sets. The observed increased

241    disorder is in agreement with the increased distortion index of the phosphate tetrahedron

242    in the Fe doped samples compared to the pure DAp. The distortion index was calculated

243    from the P-O bond lengths found from the simultaneous Rietveld refinement of the X-ray

244    and neutron diffraction patterns of the FeDAp sample series (Kyriakou et al. 2013). The

11

245  obvious modification of the induced disorder by the deuteron substitution that affects the

246  long-range order of the internal modes could be due to the additional processing (heat

247  treatment at 600 $^\circ$C during ion exchange of H with D) that would increase the disorder. In

248  any case it is worthwhile to conduct further investigation since disorder may also mark an

249  anharmonic phonon behavior.

250  In conclusion, we have studied by Raman and IR spectroscopy two sets of

251  hydroxyapatite compounds with varying degrees of atomic Fe substitution for Ca from 0

252  to 6%; one set of samples with H and the other deuterated. Only two modes were found

253  to be affected by the deuteration, related to the OH group at ~3572 cm$^{-1}$ (internal

254  stretching mode of OH) and ~631 cm$^{-1}$ (vibrational mode of Ca$_3$-OH). Iron substitution

255  for Ca did not significantly affect the frequency of the modes, but damped the intensity of

256  the internal modes substantially, whereby increasing their width. This is a clear indication

257  of increased lattice disorder with increasing degree of Fe substitution. It was also found

258  that HAp is less sensitive to disorder than the deuterated samples.

259  **Implications**

260  Although Fe is a minor substituent for Ca in the structure of physiological

261  hydroxyapatite, it affects their properties decidedly (Medeiros et al. 2002, De Vernejoul

262  et al. 1984). Motivated by the disagreement on the lattice modifications induced by the Fe

263  substitution, and a recent relevant study by combined XRD and neutron scattering on Fe-

264  and deuteron-substituted hydroxyapatite (Kyriakou et al. 2013), we have carried out

265  optical measurements on the same series of samples.

266  In this work, hematite has been detected even in samples with the smallest Fe

267  concentration, which was below the detection limits of the XRD measurements,

12

268  demonstrating the advantageous discrimination level of the Raman technique (Fig. 4). We

269  have found that Fe substitution does not affect significantly the frequency of the strong

270  modes that are related to internal vibrations of the $PO_4$ tetrahedra. On the contrary, the

271  width and the intensity of those modes were found to be very sensitive to the structural

272  disorder introduced by the Fe substitution. The disorder is related to the breaking of

273  external bonds of the $PO_4$ tetrahedra, as previously found by XRD and neutron scattering

274  (Kyriakou et al. 2013) and it is smaller in the hydroapatites compared to the deuterated

275  ones The FTIR measurements have revealed modes related to OH that challenge the

276  results of *ab initio* calculations. Our data provide substantial experimental evidence to

277  test relative theories on the lattice effects of the Fe substitution.

278

285

286

287

288

13

## References

Antonakos, A., Liarokapis, E., and Leventouri, Th. (2007), Micro-Raman and FTIR studies of synthetic and natural apatites. Biomaterials, 28, 3043-54 and references therein.

Calderin, L., Dunfield, D., and Stott, M. (2005), Shell-model study of the lattice dynamics of hydroxyapatite. Physical Review B, 72, 224304.

Corno, M., Busco, C., Civalleri, B., and Ugliengo, P. (2006), Periodic ab initio study of structural and vibrational features of hexagonal hydroxyapatite $Ca_{10}(PO_4)_6(OH)_2$. Physical Chemistry Chemical Physics, 8, 2464-72.

de Faria, D.L.A., Venancio Silva, S., and de Oliveira, M.T. (1997), Raman microspectroscopy of some iron oxides and oxyhydroxides. Journal of Raman Spectroscopy, 28, 873-8.

De Vernejoul, M.C., Pointillart, A., Golenzer, C.C., Morieux, C., Bielakoff, J., Modrowski, D., and Miravet, L. (1984), Effects of iron overload on bone remodeling in pigs. American Journal of Pathology, 116, 377-84.

Elliott, J.C. (1994) in Structure and Chemistry of the Apatites and Other Calcium Orthophosphates, Elsevier (Amsterdam, London, New York, Tokyo, 1994) and references therein.

Jiang, M., Terra, J., Rossi, A.M., Morales, M.A., Baggio Saitovich, E.M., and Ellis, D.E. (2002), $Fe^{2+}/Fe^{3+}$ substitution in hydroapatite: Theory and experiment, Physical Review B, 66, 224107.

Khudolozhkin, B.O., Urusov, V.S., and Kurash, V.V. (1974), Mössbauer study of the ordering of $Fe^{2+}$ in fluor-apatite structure. Geochemistry International, 11, 748-750.

Kyriacou, A., Leventouri, Th., Chakoumakos, B.C., Garlea, V.O., dela Cruz, C.B., Rondinone, A.J., and Sorge, K.D., (2013), Combined x-ray and neutron diffraction Rietveld

14

313    refinement in iron-substituted nano-hydroxyapatite. Journal Materials Science, 48, 3535-45

314    (2013); DOI 10.1007/s10853-013-7148-5.

315    Leventouri T, Bunaciu CE, Perdikatsis V. (2003), Neutron powder diffraction studies of

316    silicon-substituted hydroxyapatite. Biomaterials, 24, 4205–11.

317    Li ,Y., Widodo, J., Lim, S., and Ooi, C.P. (2012), Synthesis and cytocompatibility of

318    manganese (II) and iron (III) substituted hydroapatite nanoparticles. Journal Materials

319    Science, 47, 754-763.

320    Low, H.R., Phothammachai, N., Maignan, A., Stewart, G.A., Bastow, T.J., Ma, L.L., and

321    White,  T.J. (2008), The crystal chemistry of ferric oxyhydroapatite. Inorganic Chemistry,

322    47, 11774-82.

323    Martin  T.P., Merlin R., Huffman D.R., Cardona M. (1977), Resonant Two Magon

324    Raman Scattering in $Fe_2O_3$, Solid State Communications, 22, 565-7.

325    Massey  M.J., Baier U., Merlin R., and Weber W.H. (1990), Effects of Pressure and

326    Isotopic Substitution on the Raman Spectrum of a-$Fe_2O_3$: Identification of Two-Magon

327    Scattering, Physical Review B, 41, 7822–7.

328    McCarty K.F. (1988), Inelastic Scattering in a-$Fe_2O_3$: Phonon vs Magon Scattering, Solid

329    State Communications, 68, 799–802.

330    Medeiros, D.M., Plattner, A., Jennings, D., and Stoecker, B. (2002), Bone morphology,

331    strength and density are compromised in iron-deficient rats and exacerbated by calcium

332    restriction.  Journal of Nutrition, 132, 3135-41.

333    Morissay, R., Rodriguez-Lorenzo, L.M., and Gross,  K.A. (2005), Influence of ferrous

334    iron incorporation on the structure of hydroapatite. Journal Materials Science: Materials

335    in Medicine, 16, 387-92.

336    Okazaki, M., and Takahashi, J. (1997), Heterogeneous iron-containing fluoridated

337    apatites. Biomaterials, 18, 11-14.

338    Park E, Condrate RA, Sr, Lee D, Kociba K, Gallagher PK. (2002) Characterization of

339    hydroxyapatite: before and after plasma spraying. Journal Materials Science; Materials in

340    Medicine, 13, 211–218.

341    Pedone, A., Corno, M., Civalleri, B., Malavasi, G., Menziani, M.C., Segre, U., and

342    Ugliero, P. (2007), An ab initio parametrization interatomic force field for

343    hydroxyapatite. Journal of Materials Chemistry, 17, 2061-68.

344    Penel G., Leroy P.G., Rey C., and Bres E. (1998), Micro-Raman spectral study of the

345    PO4 and CO3 vibrational modes in synthetic and biological apatites. Calcified Tissue

346    International, 63, 475-81.

347    Salviulo, G., Bettinelli, M., Russo, U., Speghini, A., and Nodari, L. (2011), Synthesis and

348    structural characterization of $Fe^{3+}$ -doped calcium hydroxyapatite: role of precursors and

349    synthesis method. Journal Materials Science, 46, 910-22.

350    Shim S.H. and Duffy T.S. (2001), Raman Spectroscopy of $Fe_2O_3$ to 62 GPa, American

351    Mineralogist, 87, 318–26.

352    Srivastava, G.P. (1990), in The Physics of Phonons (Taylor and Francis, 1990).

353    Ulian, G., Valdre, G., Corno, M., and Ugliero, P. (2013), The vibrational features of

354    hydroxyapatite and type A carbonated apatite: A first principle contribution. American

355    Mineralogist, 98, 752-9.

356    Vignoles-Montrejaud M. (1984),  Contibution a 1' Etude des Apatites Carbonate es de

357    Type B. These d'Etat, Institut National Polytechnique de Toulouse

358    Wang J., White W.B., and Adair J. H. (2005), Optical Properties of Hydrothermally

359    Synthesized Hematite Particulate Pigments, Journal American Ceramic Society, 88,

360    3449–3454.

361    Wopenka, B., and Pasteris, J.D. (2005), A mineralogical perspective on the apatite bone.

362    Materials Science and Engineering C, 25, 131-143.

363    Wu, H.C., Wang, T.W., Sun, J.S., Wang, W.H., and Lin,  F.H. (2007), A novel

364    biomagnetic nanoparticle based on hydroapatite. Nanotechnology, 18, 165601-609.

365

366

367     **Figure captions**

368     Figure 1. IR spectra of iron-doped hydroxyapatites (continuous lines) and deuterated

369     oxypatites (dotted lines) for all samples in the high (a) and low (b) frequency spectral

370     region. The arrow in (b) indicates the mode that disappears with deuteration.

371     Figure 2. Raman spectra of the low (a) and high (b) frequency regions of the $x = 0.0$

372     hydroxyapatite sample with ×100 (dotted line) and ×50 (continuous line) magnification.

373     Figure 3. Raman spectra of the low (a) and high (b) frequency regions of the Fe-doped ($x$

374     $= 0.3$) hydroxyapatite sample with ×100 (dotted line) and ×50 (continuous line)

375     magnification.

376     Figure 4. (a) Raman spectra of the FeDAp samples (low frequency region). Straight lines

377     indicate the peaks due to the $\alpha$-$Fe_2O_3$ phase and arrows the Raman modes of the apatite.

378     (b) The dependence on the Fe nominal atomic substitution of the new modes attributed to

379     the hematite phase.

380     Figure 5. Raman spectra of FeHAp (continuous lines) and FeDAp (dotted lines) for all Fe

381     concentrations. All spectra have the same scale presented on the vertical axis.

382     Figure 6. The dependence on Fe concentration of the intensity (squares, left axis) and

383     width (crosses, right axis) of the $v_1$ mode of FeHAp (a) and FeDAp (b).

384     Figure 7. The dependence on Fe concentration of the intensity for two of the strong $v_3$

385     modes, v3-1 (squares) at ~1027 cm$^{-1}$ and v3-3 (crosses) at ~1046 cm$^{-1}$ of FeHAp (a) and

386     FeDAp (b).

387

388    Table 1. Samples studied, corresponding phase identification, and identified phases (from

389    Kyriakou et el. 2013).

| File names of hydroxyapatite | Chemical formula | File names of deuterated apatites | Nominal Fe content $x$ | Identified impurity phases (from Kyriakou et el. 2013) |
|---|---|---|---|---|
| FeHAp0 | $Ca_5(PO_4)_3OH$ | FeDAp0 | 0.00 | |
| FeHAp005 | $Ca_{4.95}Fe_{0.05}(PO_4)_3OH$ | FeDAp005 | 0.05 | |
| FeHAp01 | $Ca_{4.90}Fe_{0.10}(PO_4)_3OH$ | FeDAp01 | 0.10 | |
| FeHAp02 | $Ca_{4.80}Fe_{0.20}(PO_4)_3OH$ | FeDAp02 | 0.20 | $\alpha$-$Fe_2O_3$ |
| FeHAp03 | $Ca_{4.70}Fe_{0.30}(PO_4)_3OH$ | FeDAp03 | 0.30 | $\alpha$-$Fe_2O_3$ |

390

391    Table 2. Raman and IR modes  and their assignments.

| Mode frequency ($cm^{-1}$) | Detected in the compounds | Spectroscopic method | Assignment (Elliott 1994; Antonakos et al. 2007) |
|---|---|---|---|
| 223, 244, 291, 409, 612, 1320 | all with Fe, increase with Fe | Raman | $\alpha$-$Fe_2O_3$ (Hematite) |
| 839, 894, 916, 925 | all | Raman | $v_4$ $CO_3$ and/or $HPO_4^{2-}$ impurities |
| 566, 600 | all | IR | $v_4$ $PO_4$ |
| 631 | FeHAp | IR | $Ca_3$-$(OH)$ |

19

| | | | librational OH mode |
|---|---|---|---|
| 963 | | IR | $v_1$ PO$_4$ |
| 1026, 1088 | all | IR | $v_3$ PO$_4$ |
| 2633 | FeDAp | IR | OH |
| 3572 | FeHAp | IR | OH |
| 330 (very weak) | Dap, HAp | Raman | Ca$_3$-(OH)? |
| 431, 448 | all, decrease with Fe content | Raman | $v_2$ PO$_4$ |
| 581, 593, 610, 617 | all, decrease with Fe content | Raman | $v_4$ PO$_4$ |
| 962 | all, decrease with Fe content | Raman | $v_1$ PO$_4$ |
| 1027, 1040, 1046, 1075 | all, decrease with Fe content | Raman | $v_3$ PO$_4$ |
| 1252, 1297 | all | Raman | CO$_3$ , amide and/or HPO$_4^{2-}$ impurities |

392

20
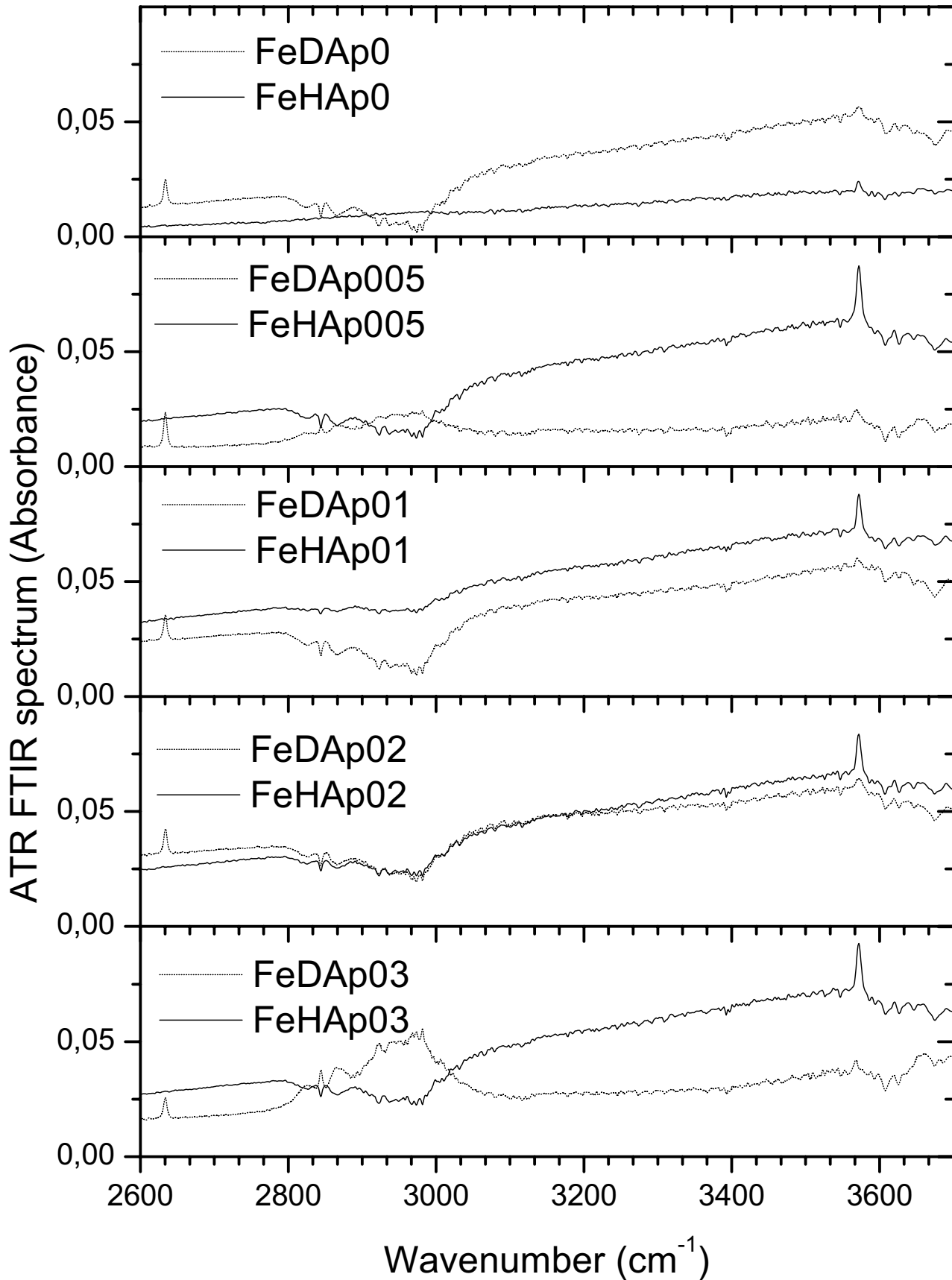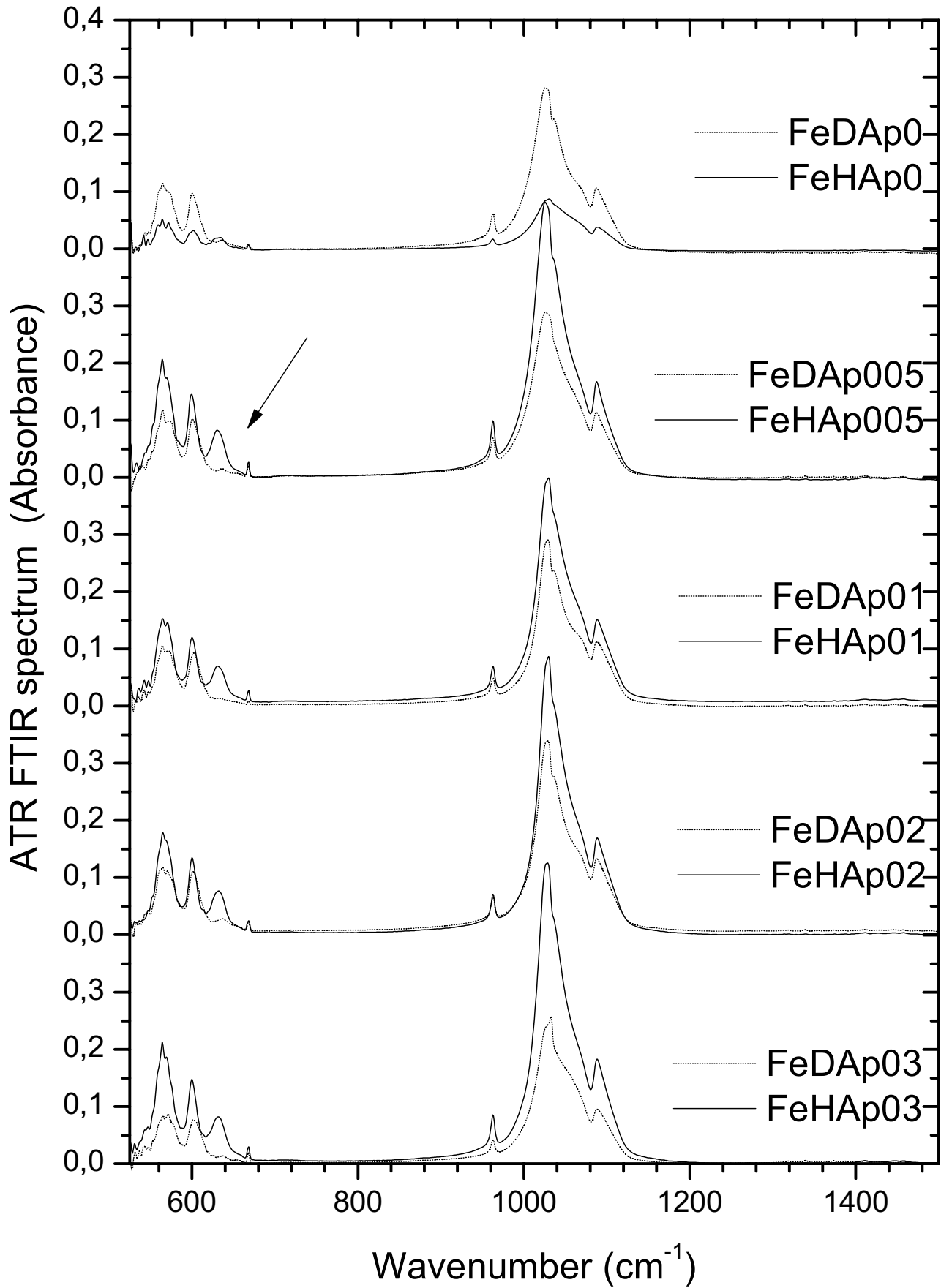
Figure 1a

Figure 1b
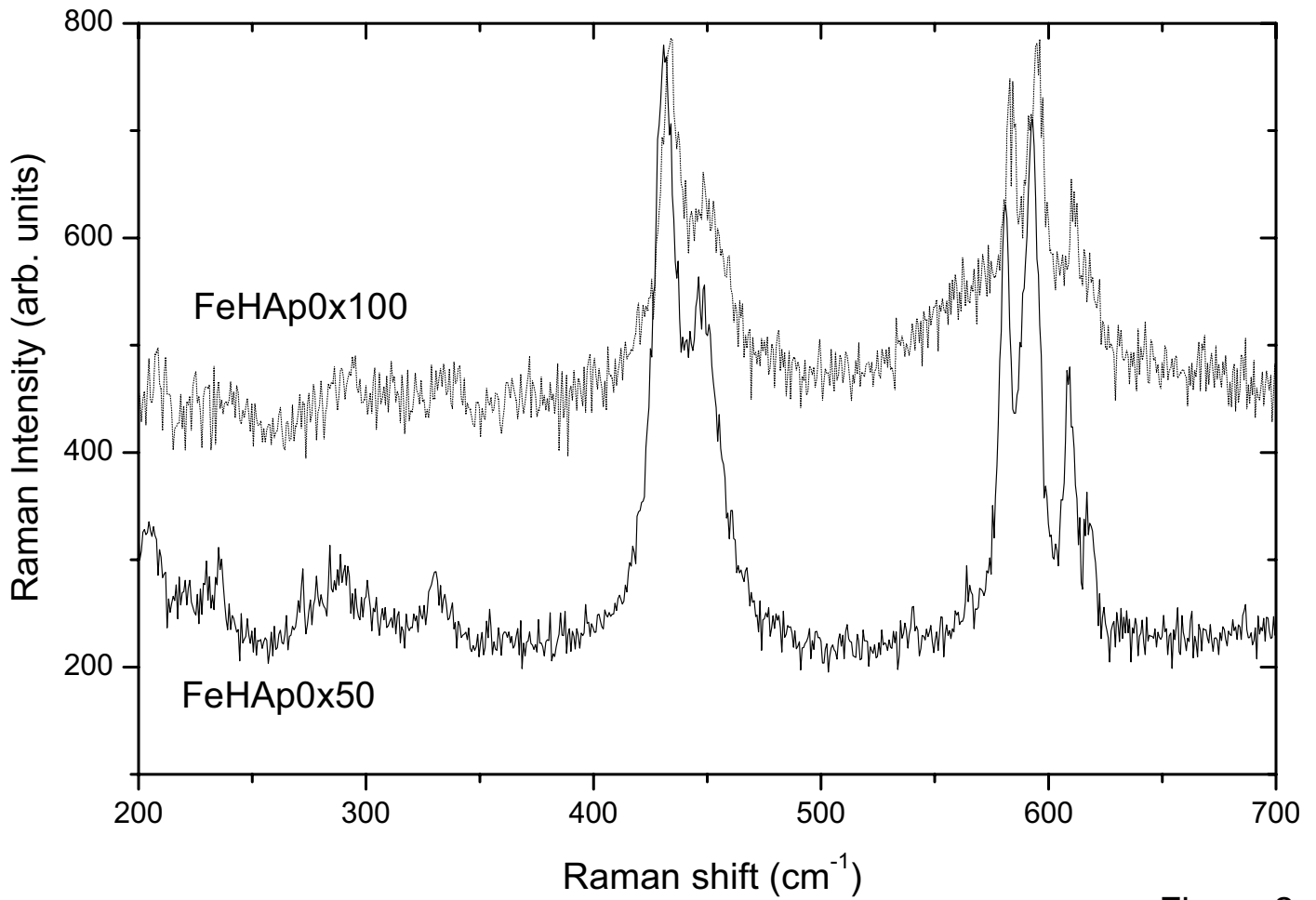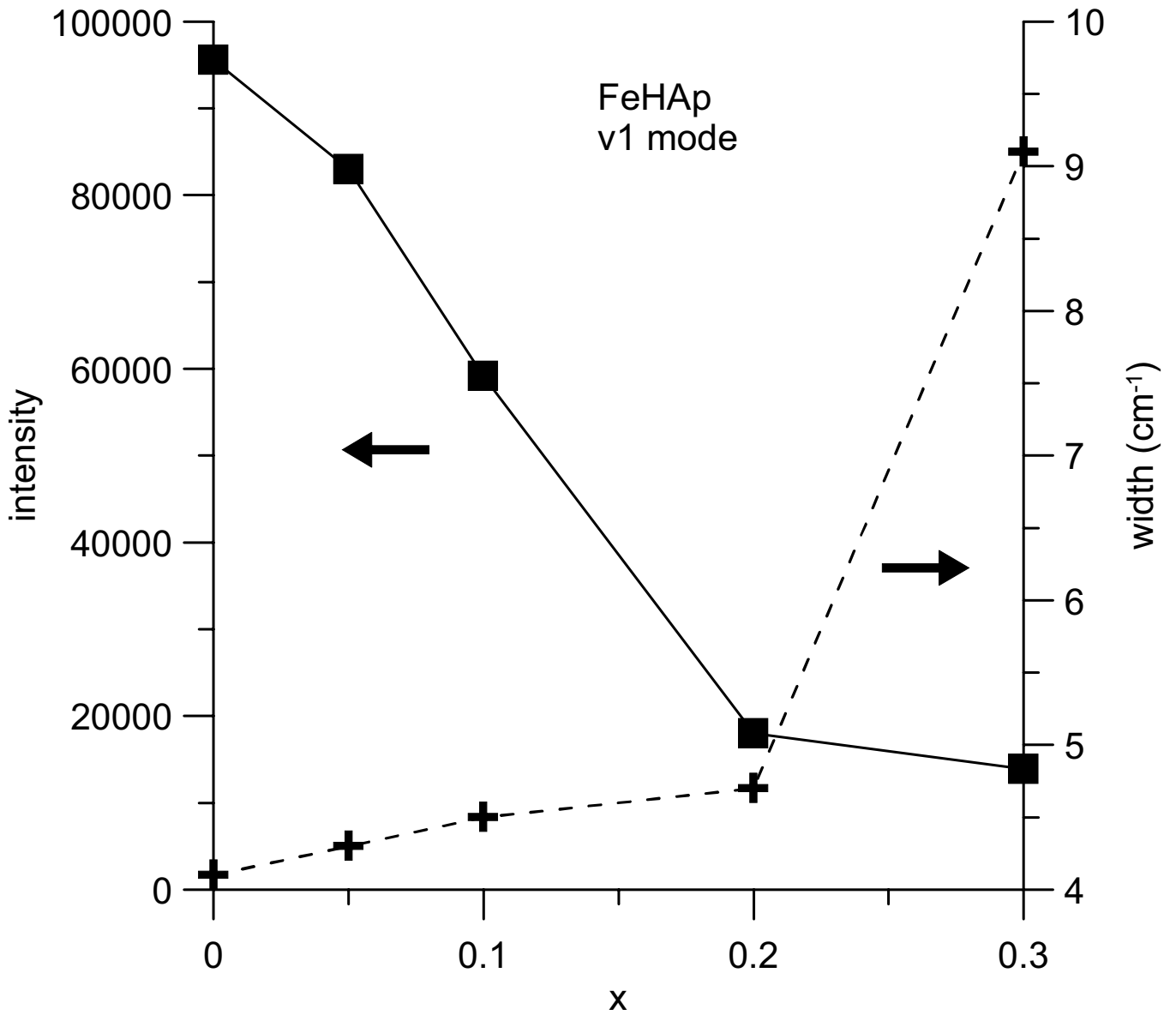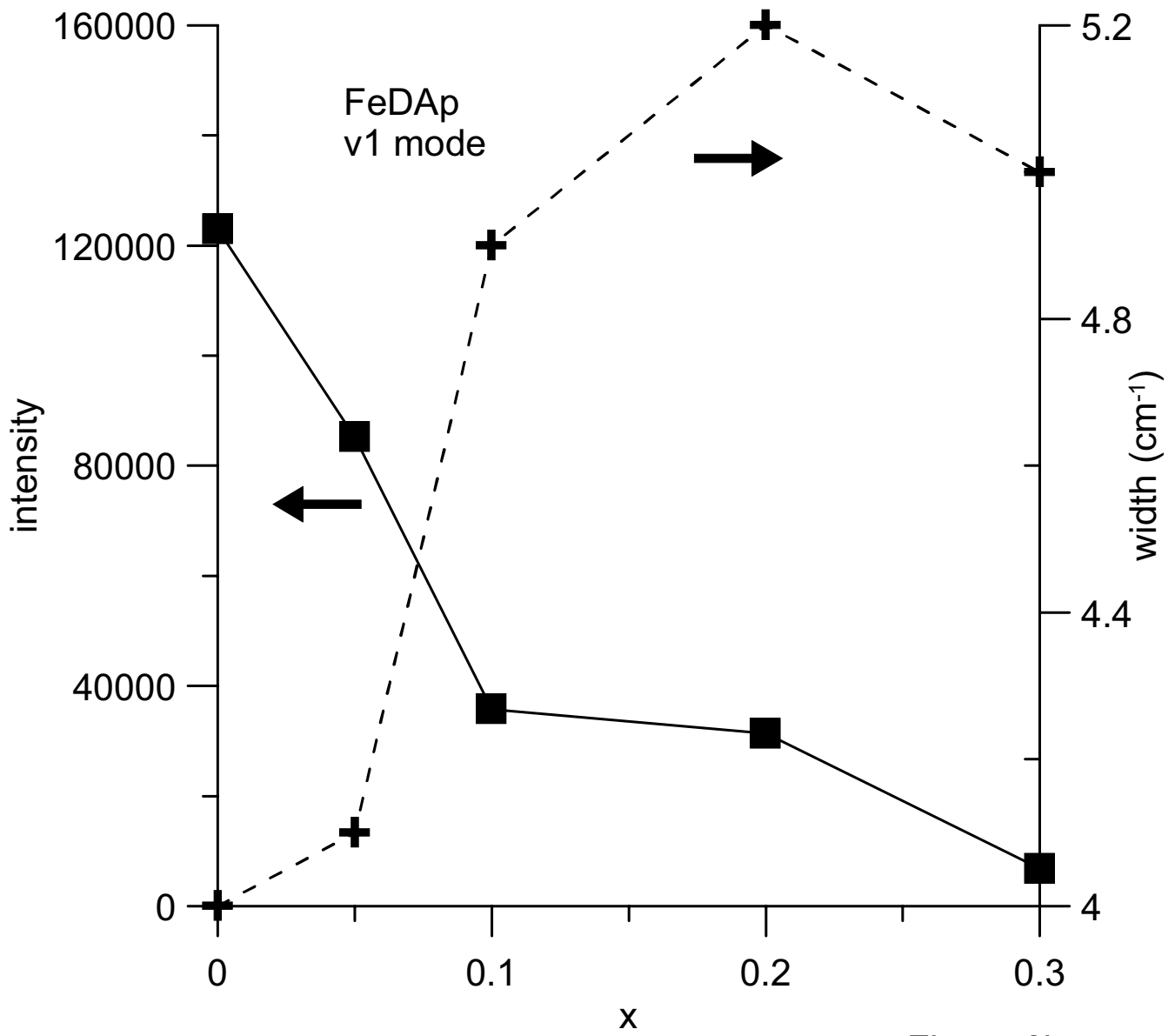
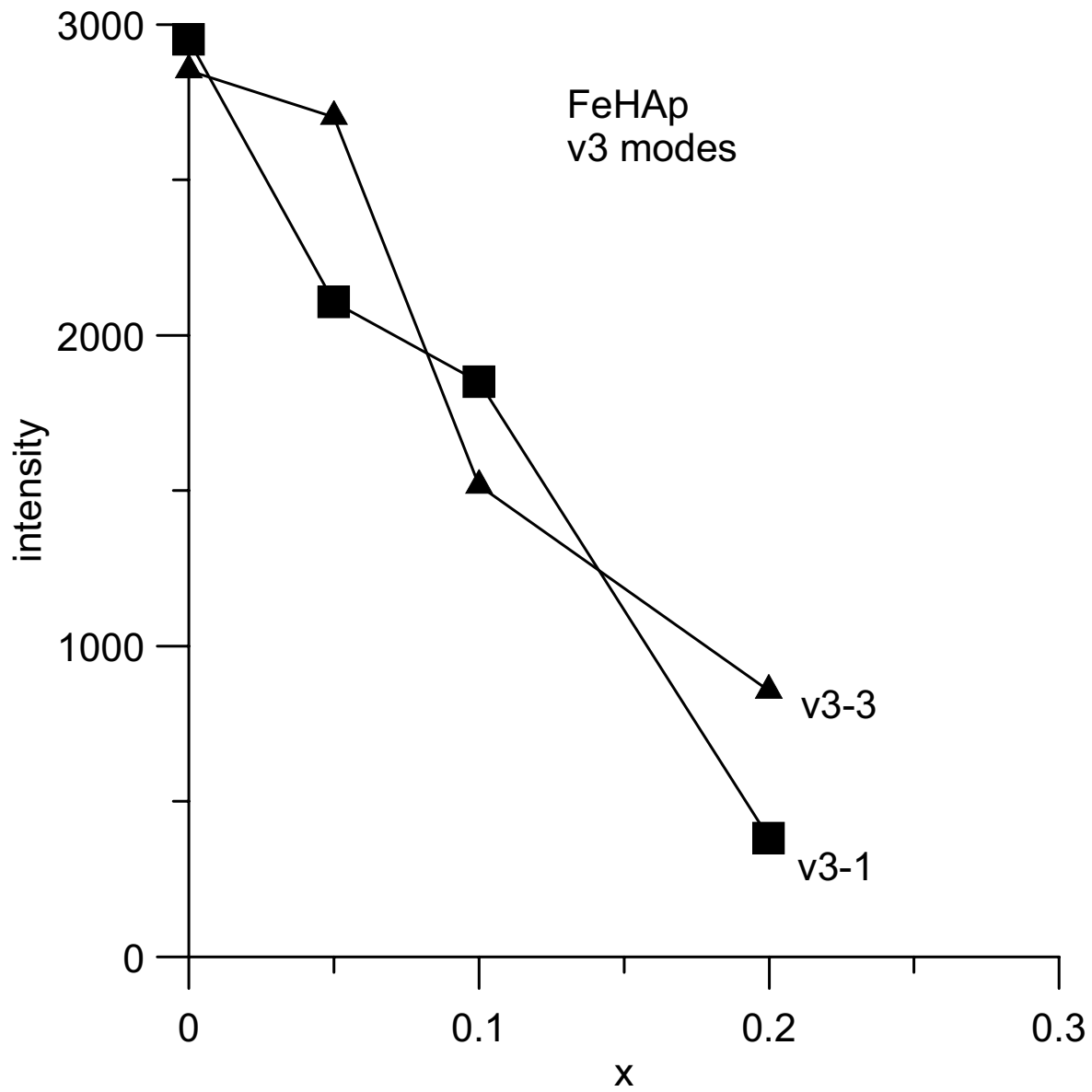Figure 2a
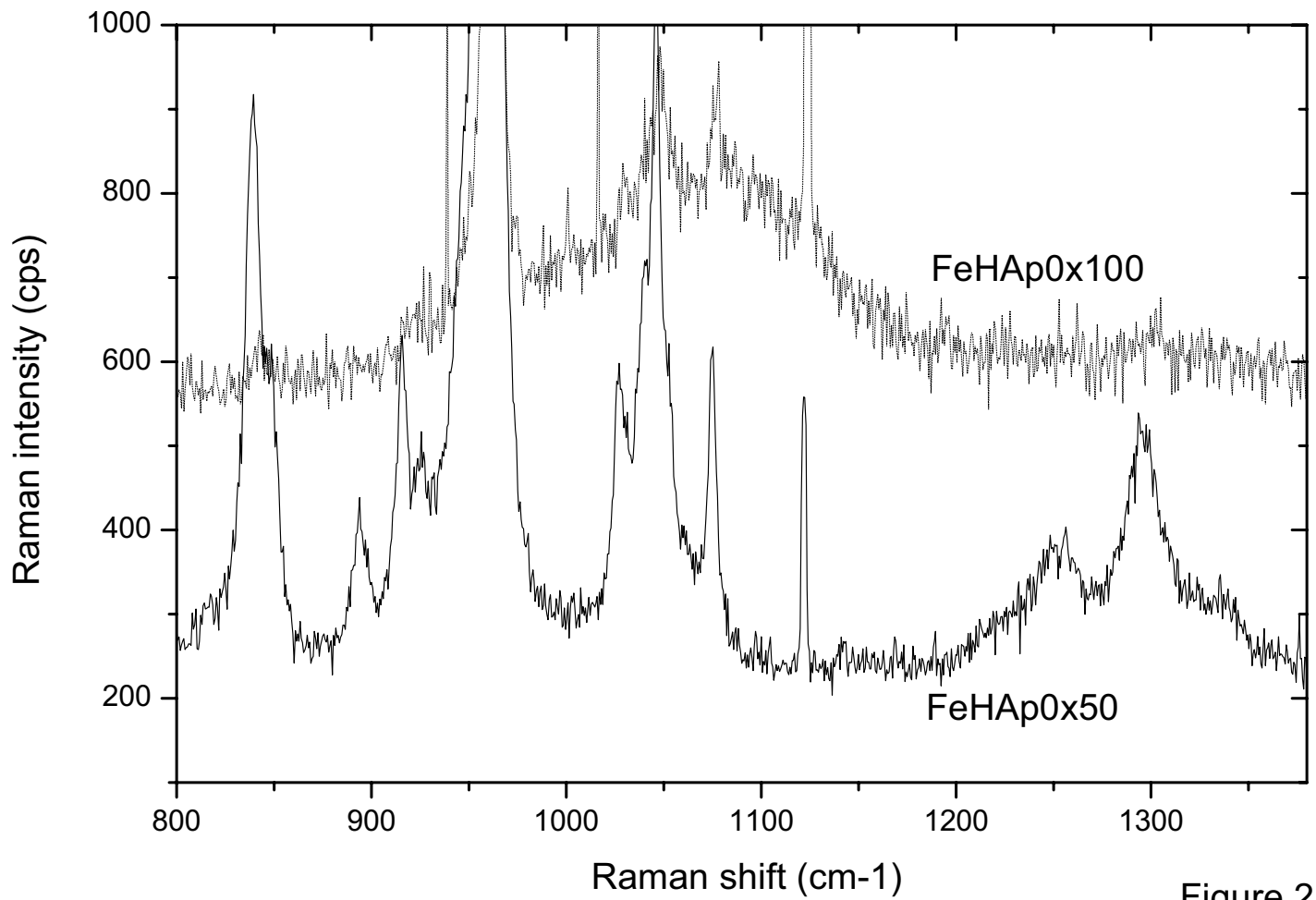
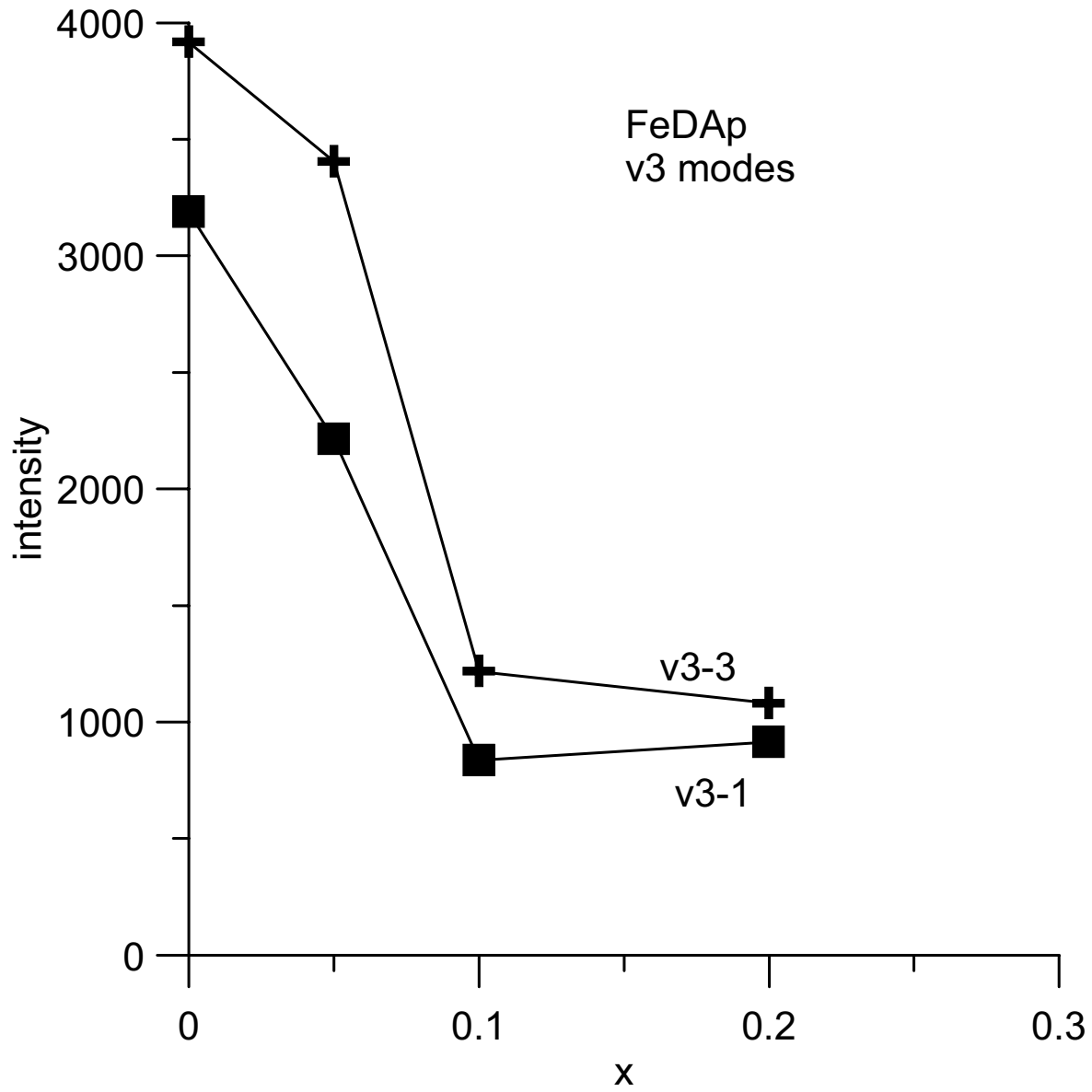Figure 2b
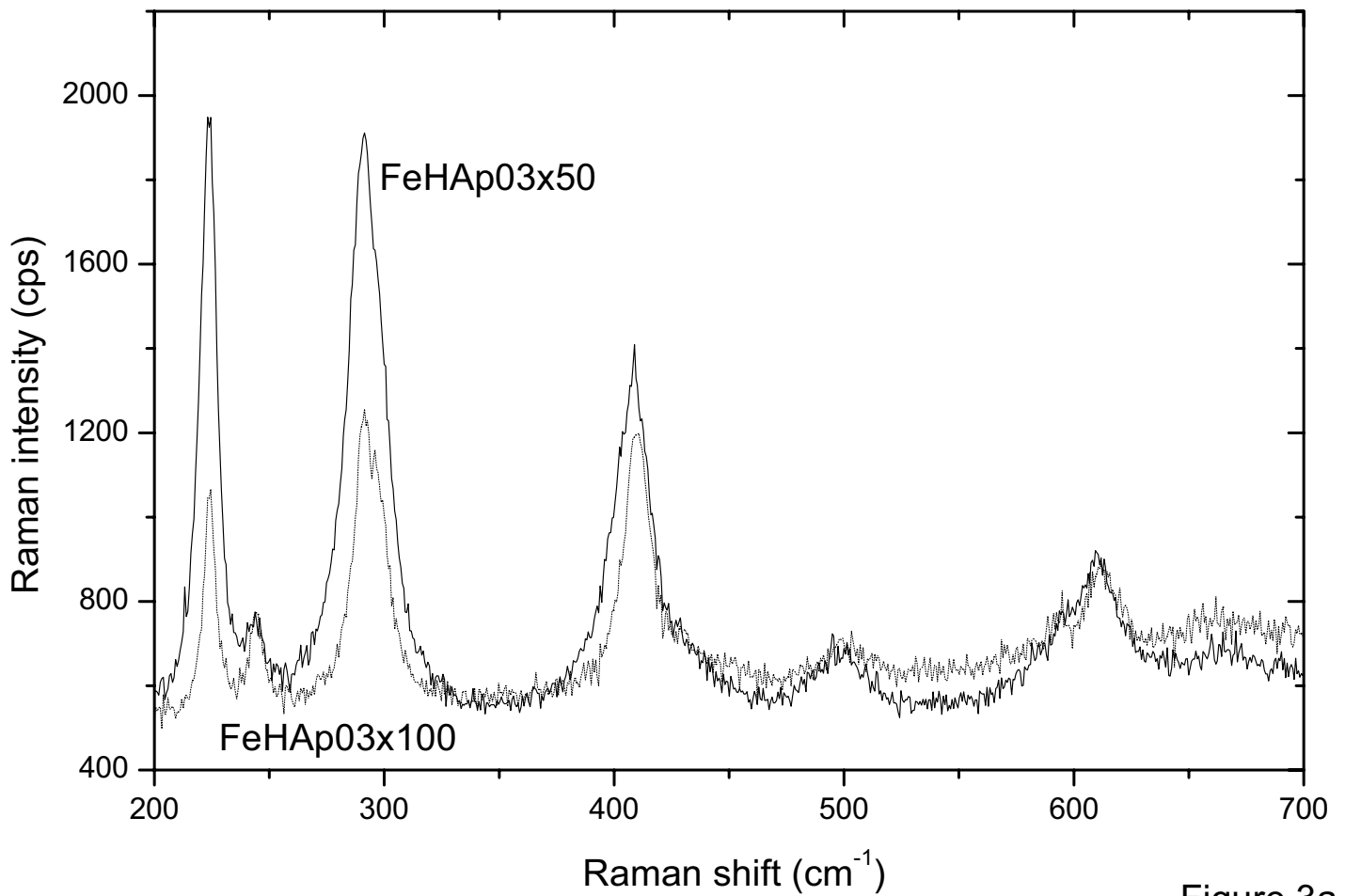
Figure 3a
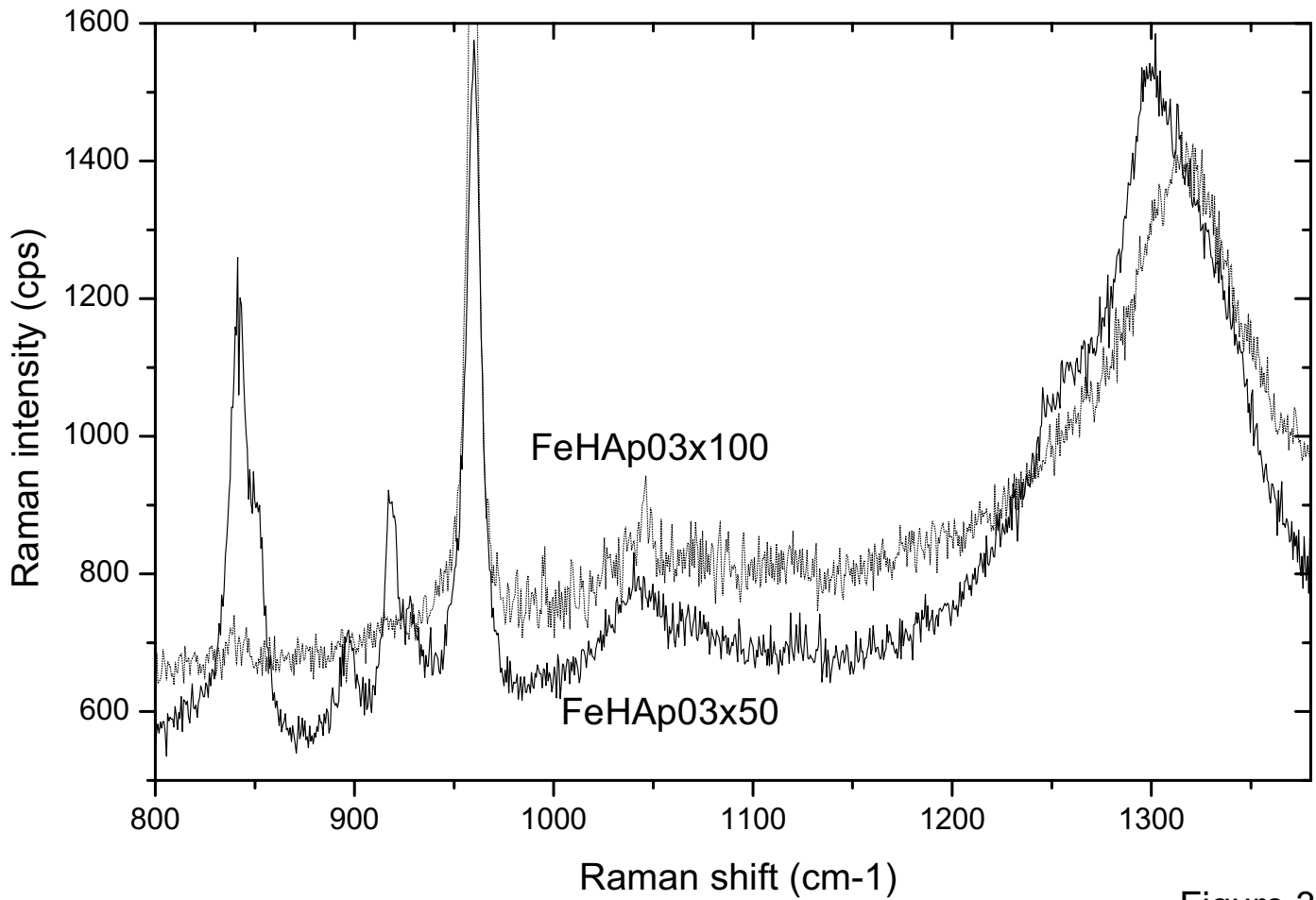
Figure 3b
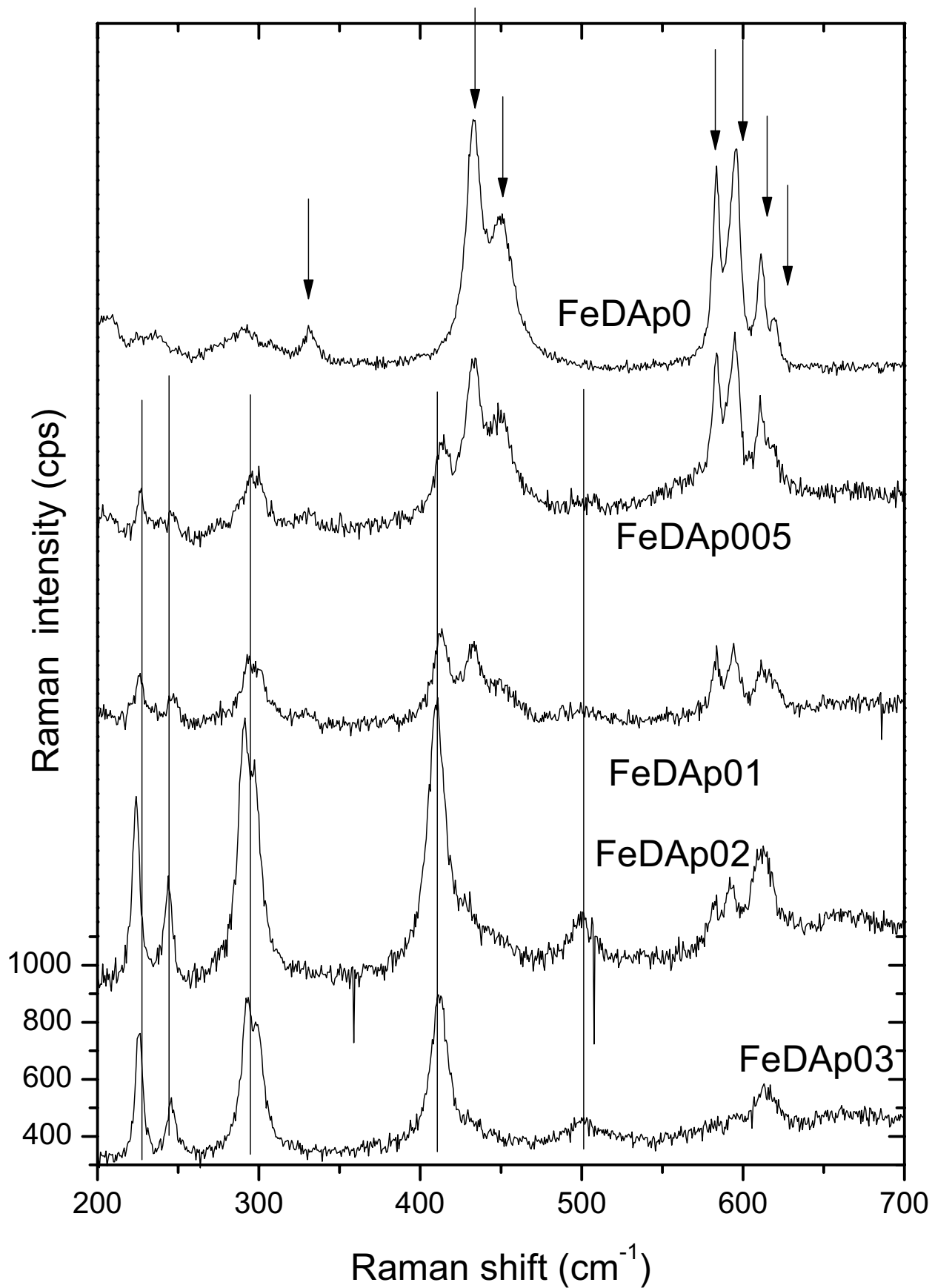
Figure 4a
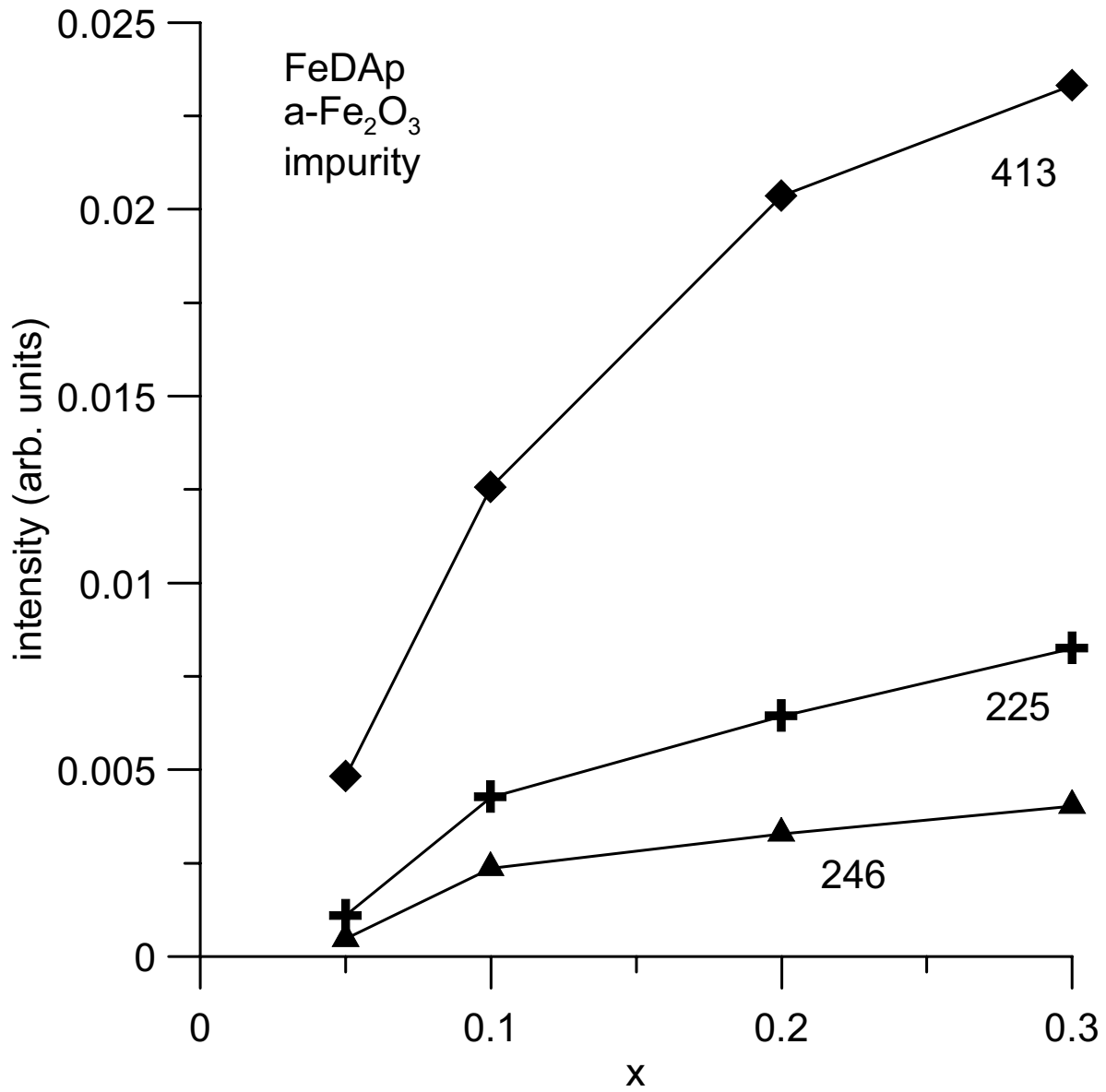
Figure 4b
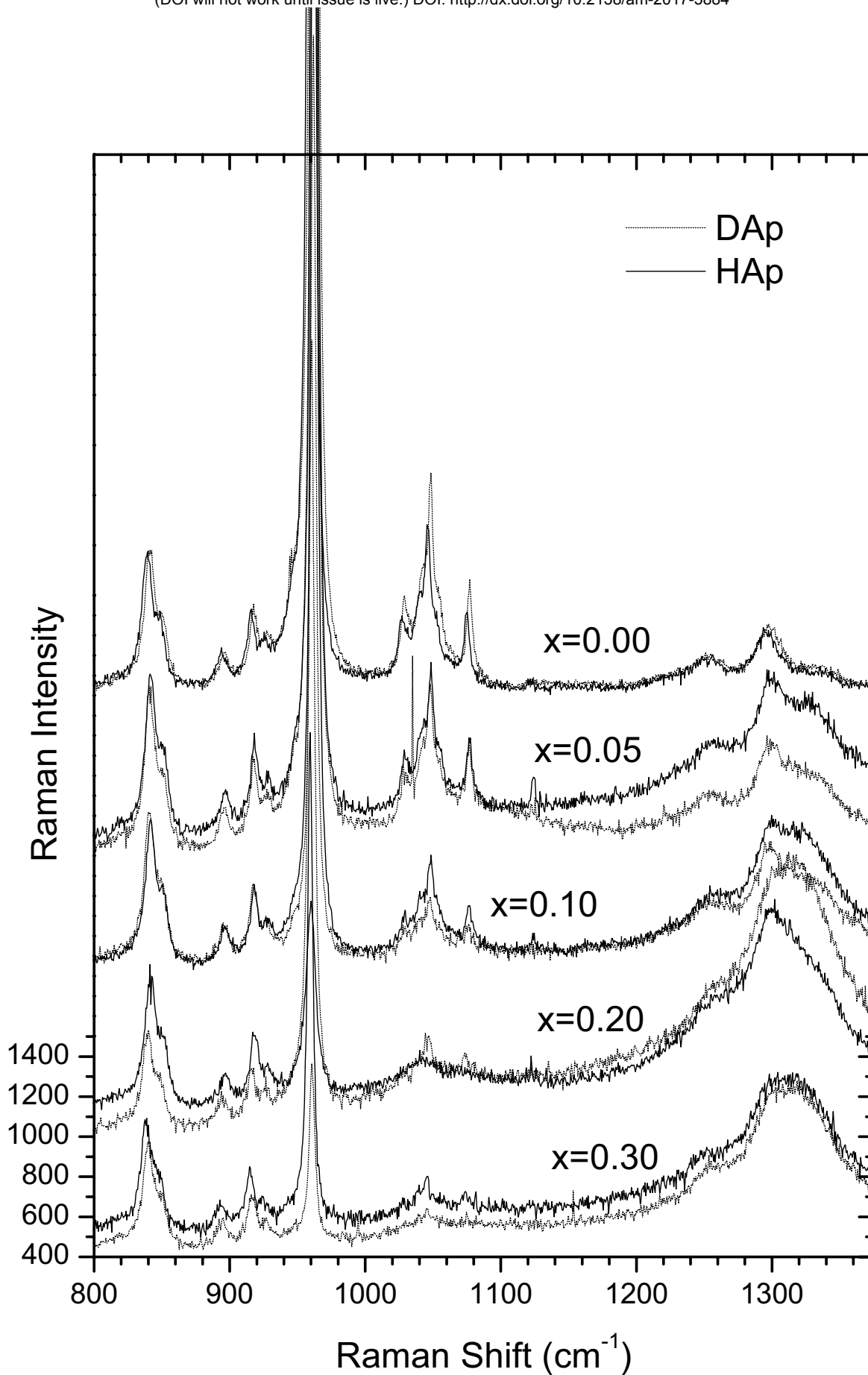
Figure 5

Figure 6a

Figure 6b

Figure 7a

Figure 7b